A field operational test on valve-regulated lead-acid absorbent-glass-mat batteries in micro-hybrid electric vehicles. Part I. Results based on kernel density estimation

S. Schaeck[a,*], T. Karspeck[a], C. Ott[a], M. Weckler[b], A.O. Stoermer[a]

[a] *BMW Group, 80788 München, Germany*
[b] *EVA Fahrzeugtechnik GmbH, 80939 München, Germany*

ARTICLE INFO

ABSTRACT

In March 2007 the BMW Group has launched the micro-hybrid functions brake energy regeneration (BER) and automatic start and stop function (ASSF). Valve-regulated lead-acid (VRLA) batteries in absorbent glass mat (AGM) technology are applied in vehicles with micro-hybrid power system (MHPS). In both part I and part II of this publication vehicles with MHPS and AGM batteries are subject to a field operational test (FOT). Test vehicles with conventional power system (CPS) and flooded batteries were used as a reference. In the FOT sample batteries were mounted several times and electrically tested in the laboratory intermediately. Vehicle- and battery-related diagnosis data were read out for each test run and were matched with laboratory data in a data base. The FOT data were analyzed by the use of two-dimensional, nonparametric kernel estimation for clear data presentation.

The data show that capacity loss in the MHPS is comparable to the CPS. However, the influence of mileage performance, which cannot be separated, suggests that battery stress is enhanced in the MHPS although a battery refresh function is applied. Anyway, the FOT demonstrates the unsuitability of flooded batteries for the MHPS because of high early capacity loss due to acid stratification and because of vanishing cranking performance due to increasing internal resistance. Furthermore, the lack of dynamic charge acceptance for high energy regeneration efficiency is illustrated. Under the presented FOT conditions charge acceptance of lead-acid (LA) batteries decreases to less than one third for about half of the sample batteries compared to new battery condition. In part II of this publication FOT data are presented by multiple regression analysis (Schaeck et al., submitted for publication [1]).

© 2010 Elsevier B.V. All rights reserved.

1. Micro-hybrid electrical power system

In March 2007 the BMW Group has introduced micro-hybrid functionalities in large-scale series vehicles in order to reduce fuel consumption and CO$_2$ emissions of modern passenger cars. The micro-HEV (hybrid electric vehicle) acts as lowest level of vehicle powertrain electrification [2]. This electrification is based on brake energy regeneration (BER) and the automatic start and stop function (ASSF) of the internal combustion engine (ICE), which are implemented in the conventional 14 V power system (CPS) with only little modifications [2,3]. The fuel saving potential of the micro-hybrid power system (MHPS) reaches to about 6% in the New European Driving Cycle [5–7].

In micro-HEVs ASSF switches off the engine at idle. Then, the battery supplies electric power instead of the belt-driven alternator. The ICE is restarted automatically on demand of the driver by hitting the clutch [3]. At a minimum engine-off time period of 5 s the ICE stop results in effective fuel saving [5].

The novelty of BER is caused by the fact that the alternator control is directly linked to specific driving phases of the vehicle like traction or braking. During coasting and braking the rotational speed of the alternator is not powered by fuel consumption, but by the vehicle inertia moment. The BER function

---

Abbreviations: AGM, absorbent glass mat; AM, active mass; ASSF, automatic start and stop function; BER, brake energy regeneration; C_{20}, 20 h-capacity; CA, charge acceptance; C_{act}, actual 20 h-capacity (maximum available capacity); C_{nom}, nominal 20 h-capacity; CCA, cold crank amps; CPS, conventional power system; DCA, dynamic charge acceptance; EM, energy management; f, probability density; fc, full cycle; FOT, field operational test; HEV, hybrid electric vehicle; IBS, intelligent battery sensor; ICE, internal combustion engine; LA, lead-acid; MHPS, micro-hybrid power system; NE, negative electrode; OEM, original equipment manufacturer; pSoC, partial state-of-charge; SLI, starting, lighting, ignition; SoC, state-of-charge; SQL, standard query language; t_{6V}, time after reaching 6 V battery voltage at 0.6 CCA acc. to [15]; TDA, tear-down analysis; t_{rest}, rest time; U_{10s}, voltage after 10 s application of CCA acc. to [15]; VIP fleet, vehicle fleet for special events; VRLA, valve-regulated lead-acid.

* Corresponding author. Tel.: +49 89 382 78653; fax: +49 89 382 42827.
E-mail address: stefan.schaeck@bmw.de (S. Schaeck).

controls the alternator output to elevated charge voltage resulting in 'boost' charging without emission of CO_2. At a later time period the regenerated energy is fed back to the power net; less fuel is consumed due to reduced power output of the alternator [7].

ASSF and BER are part of an intelligent onboard energy management (EM), which controls energy and communication flow in the vehicle power net. Hereby, the lead-acid (LA) battery is equipped with the intelligent battery sensor (IBS) for logging battery voltage, current and temperature. These parameters are critical for battery monitoring and the ASSF/BER software.

The operational strategy of the LA battery in the MHPS marks a paradigm shift. The battery does not only fulfil SLI functions with the objective of full state-of-charge (SoC). Instead, intelligent EM uses the battery as 'active' component, which is linked to the operational mode of the car like idling, cranking and braking. Furthermore, the battery is controlled to be at partial SoC (pSoC) in order to enable maximum charge acceptance during regeneration [8].

The LA battery is the key component in the MHPS for two reasons: firstly, SLI batteries have always been the main reason for vehicle breakdowns in automotive history as their cycle life is shorter than the vehicle service life time [9]. Secondly, the novel operational strategy results in even tougher battery requirements. For that reason the BMW Group does not apply conventional 12 V LA batteries in flooded technology, but valve-regulated LA batteries (VRLA) from different suppliers with absorbent glass mat (AGM) separators (latest development maturity level of early 2007). The cycle stability is about three times better, they accomplish higher charge acceptance, provide higher power density and are more robust against pSoC-operation. As a result, VRLA–AGM batteries are more durable and meet the specific challenges in the MHPS in a better way [10].

These challenges are shortly described in the following:

(a) *Cyclability*: Energy throughput is inherently increased by ASSF and BER. This was proven by field analysis in [3]. Cycling (in number of full cycles per 1000 km) was increased by 30% in the MHPS compared to the CPS in BMW vehicles with four-cylinder engine and manual transmission (configuration at MHPS launch). This strongly favours VRLA–AGM batteries since these are more durable in cycling operation compared to flooded batteries by a factor of three (derived from the 17.5% depth-of-discharge cycling test). By design optimizations flooded batteries could be designed to cycle life above 150 fc [11]. However, this would result in an energy optimized battery which is not only aimed at in the MHPS.

(b) *Warm cranking performance*: The ASSF function results in frequent high-rate battery discharges. The battery has to provide power reliably and rapidly whereby the accompanied voltage drop should be as small as possible for reasons of power net stability [12]. This is synonymous to low battery internal resistance and to a power optimized design, respectively. The increase of the internal resistance over life time is expected to be kept at a minimum.

(c) *Dynamic charge acceptance* (*DCA*): In this context the term 'charge acceptance' does not mean fast charging at low temperature from low SoC levels, but high boost charge current at short time scale at elevated charge voltage. The dynamic charge acceptance has been a subsidiary parameter in LA battery technology [13] and is influenced by several factors, especially the previous operational history of the battery [10,13].

(d) *Operation at pSoC*: A major challenge for LA batteries in the MHPS is the partial discharge. It was reported in [3] by field data analysis of MHPS vehicles, that the temporal SoC distribution is shifted to lower SoC by 8% compared to CPS vehicles

on average. This strongly depends on the special use case and may differ with model type and OEM, of course. The permanent depletion of charge may result in enhanced hard sulphation of the negative electrode of the tested batteries [14]. Decreased dynamic charge acceptance and capacity are the consequences. In order to overcome this aging process, VRLA–AGM batteries are periodically fully charged by an onboard 'refresh' function [3]. The positive effect of refreshing in terms of charge acceptance and capacity loss is addressed in [3]. The refresh is realized as pulsed charging with 14.8 V as upper charge voltage, which is temperature-independent because of higher dissolubility of sulphate crystals at elevated voltage and temperature [4]. The refresh is ideally started before the transition from reversible to irreversible sulphation has occurred. This is realized by an algorithm with several input parameters like cycling, rest time, SoC and calendar time. The refresh is associated with a charge factor of about 1.1.

In this publication VRLA–AGM batteries in the MHPS are scope of a field operational test (FOT). Statistical data on short term operational behaviour and long term degradation phenomena can be derived from the FOT as will be described in the following sections.

2. Battery field operational test on series and pre-series vehicles

A FOT is part of the simultaneous engineering (SE) process in automotive industry. It is at the end of the product development process and may overlap with series production. Thus, the FOT aims at the final complete system with possibly little modifications. Pre-series vehicles and series vehicles of four different fleets were part of the presented FOT (all BMW cars):

(a) Police cars operated in the Munich region served as reference group with CPS, both flooded and VRLA–AGM batteries were mounted. The mileage performance, i.e. average mileage per day, was rather inhomogeneous; both extended parking times and continuous operation occurred. The vehicles were equipped with different engine types.

(b) Mobile service cars (only 6-cylinder Diesel engines) are operated as 'automobile roadway repair vehicles' and are equipped with an electric onboard diagnose system.

(c) Energy throughput per operating hour was rather high. Flooded and AGM batteries were mounted and conventionally operated.

(d) VIP shuttle-service cars (VIP fleet) were vehicles with CPS or MHPS. Both flooded and VRLA–AGM batteries were mounted. The driving profile in this fleet was comparable to customer driving profiles.

(e) Pre-series vehicles were equipped solely with VRLA–AGM batteries in combination with the MHPS. Optionally, vehicles with only BER were used (only pSoC operation, no ASSF). The mileage performance was very high, so that vehicle rest times were not sufficiently represented in this fleet. However, a few vehicles were operated in special driving profiles, which is scope of part II of this publication [1].

The number of involved MHPS vehicles was comparable to the number of CPS vehicles. The number of tested VRLA–AGM batteries was larger than the number of flooded batteries. Since the FOT is aimed at investigation of LA batteries in the MHPS, a single battery was either strictly allocated to operation in either CPS vehicles or in MHPS vehicles. The large majority of batteries was mounted in the trunk.
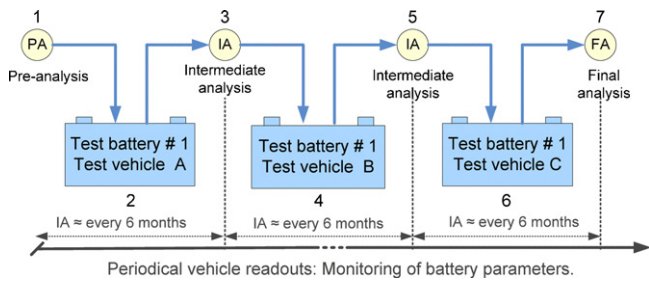
Fig. 1. Rotation-based FOT: a test battery was mounted in several test vehicles with intermediate electrical analysis in the laboratory. This test design was more practicable compared to a vehicle-related design where each test battery is assigned to a specific test vehicle.

2.1. Organization of the FOT

The FOT was based on a 'rotation principle', i.e. a test battery may have been operated in several different vehicles (Fig. 1). After an electrical pre-analysis in the lab (acquisition of fundamental battery parameters like C_{20}, $U_{10\,s}$, $t_{6\,V}$, etc.) the test battery was mounted in the first test vehicle [15]. After an aspired operational time of about six months the test battery was dismounted and electrically tested again (intermediate analysis, see Fig. 1). Only in case of more than about 70% remaining maximum capacity ($C_{act} > 70\% \cdot C_{nom}$) the battery was released for further vehicle operation. Otherwise a final electrical analysis and a TDA (optional) were performed. It has to be mentioned that a C_{20} measurement was part of the intermediate analysis. It was shown in [3] by bench test experiments that a C_{20} has serious influence on further battery behaviour in terms of slowed degradation. This implies a hardly quantifiable inaccuracy of the presented FOT and may limit its representativeness for random sample realization of the customer field.

Most of the involved vehicles delivered detailed battery-related information by the vehicle diagnose system. Both the error and the info memory were read out in the course of mounting and dismounting the test batteries. Thus valuable battery parameters could be gathered for interpretation of the FOT like, e.g. cycling rates, SoC distribution, temperature distribution, rudimentary driving behaviour, etc.

All information of the FOT were joined in an own data base. This was structured according to 'test-IDs' representing each test run of a certain battery in a certain vehicle with all vehicle-related information and 'battery-IDs' representing each test battery with acquired laboratory data. The available information in the data base for this publication included 320 test batteries, 544 test vehicles and 14,176,476 driven test kilometres. This proves the high statistical relevance of the presented FOT. However, it will be seen by the results that the complexity of the tested system ('electrochemical energy storage device integrated in the automotive power net and operated by a customer') requires a huge sample space in order to gather significant interpretation. Furthermore, a battery FOT should ideally cover the entire battery service life time. This is also hard to fulfil in a representative way since battery degradation usually occurs on the time scale of years and, ultimately, results in a vehicle breakdown, which was not provoked in this FOT.

3. Data evaluation

The structure of the FOT data base enabled automated data exporting of the operational history of each single battery by combining lab-related and vehicle-related information. An example is given in Fig. 2 for a battery, which was operated in the CPS (squares) (three test runs in CPS vehicles with pre-analysis, two intermedi-
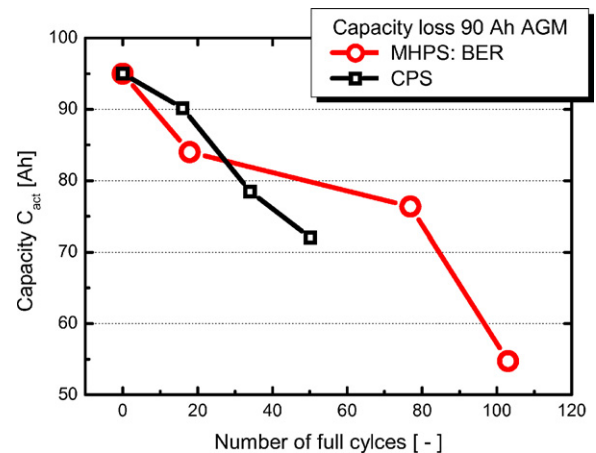
Fig. 2. Example of operational resumes as extracted from the FOT data base for two particular batteries. The capacity loss is given versus cycling whereby the full cycles from each test run are accumulated. For example, the second test run of the MHPS test run contributed with about 60 full cycles.

ate analyses and final analysis in the laboratory) in comparison to a battery operated in the MHPS (circles). It has to be noted that the number of full cycles in Fig. 2 is accumulated. Thus, by depicting the C_{20} capacity at the ordinate, the loss of capacity can be illustrated versus total battery cycling. Such a 'battery resume' cannot be recorded onboard. Improved onboard battery monitoring systems are under development (e.g. [16]) and are mainly aimed at software algorithms and operational techniques, which (implicitly) indicate battery key parameters, e.g. onboard impedance spectroscopy [17].

In order to give interpretations on the specific operational characteristics of LA batteries in the MHPS, a representative statistical sample of FOT batteries had to be evaluated as performed in Fig. 2. However, scatter plots are not practical for statistical analysis because they provide only limited information on (multi-)trends and deviations from those as well as variations in general. Large sample sizes and data scattering make the illustrations quite unclear and it is only hardly possible to present two independent data sets in one plot. An adequate technique of visualization could have been accomplished by 3D-histograms. However, plotting 3D-histograms in the 2D-plane often hides information. Alternatively, the histograms can be converted into colour-coded, topographic maps. The next section suggests a similar data evaluation method on the basis of probability distribution estimates.

Strong data scattering is an inherent property of a battery FOT due to the complexity of the system as mentioned above. Thus, any systematic error had to be necessarily avoided for not to make the results more inexact in addition. Therefore, several quality indices were linked to each battery test-ID. Only if an automated plausibility check as part of SQL queries on the data base was OK, a battery test run could be exported from the data base. Examples for implausible test runs occurred, e.g. if the vehicle readout protocol was not errorless or if the time period between battery dismounting and the intermediate analysis in the laboratory exceeded three weeks.

3.1. Overview: kernel density estimation

The two-dimensional, nonparametric kernel density estimation is an adequate method for presenting statistical distributions. It avoids the bin-width dependence of illustrations using histograms. Frequencies are presented as smooth functions. Probability densities and estimates of these have several advantageous properties: As integrals of probability densities are normalized, the distance between the associated contour plot lines, which indicate the corresponding heights, serves as an indicator for variation of the
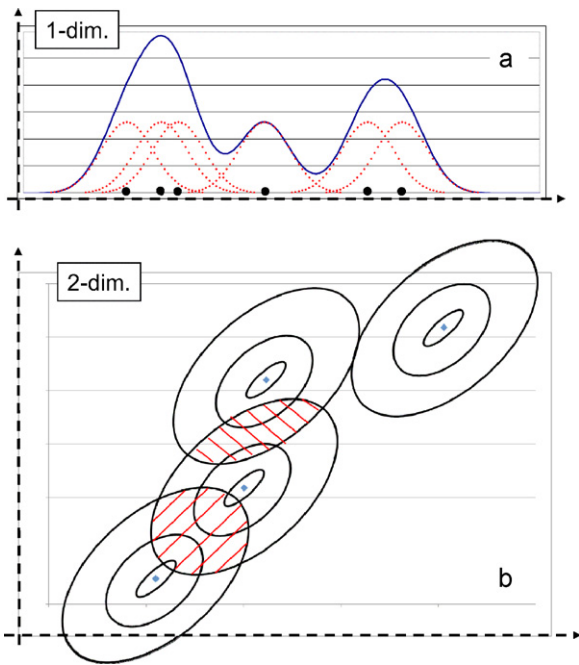
Fig. 3. (a) Kernel density estimation as the sum of kernel functions (here: Gaussian curves, dotted) associated to six sample data points (dots on abscissa). (b) Two-dimensional kernel density estimation. Four exemplary data points (hash symbols) and contour lines of the associated orientated kernel (solid lines). Areas with increased density due to summation of kernels are shaded red (density increased in comparison to the contribution of only one kernel). (For interpretation of the references to colour in this figure legend, the reader is referred to the web version of the article.)

probability density. Moreover, main directions of variation can be recognized. Most important, trends and the deviation from these can be displayed as well as multi-trends, which could not be resolved satisfyingly by approaches containing dependencies based on a function (i.e. regression). In addition, large sample sizes do not affect the complexity of the visualization. Using probability density estimates allows for the visualization and comparison of statistical data in a suitable manner.

An overview of the method is discussed in the following; it is summarized by Karspeck et al. [18]. The nonparametric distribution estimation provides information about the underlying population of an experiment by using the information of a sample realization. In non-random-sample environments an adequate visualization of the data, which exhibits advantages over scatter plots and histograms, is provided by methods of nonparametric distribution estimation.

The basic idea of kernel density estimation and extensions to these, which are valuable for applications, is briefly introduced: the probability density f of a random variable $\mathbf{X}$ at $\mathbf{x} \in \mathbb{R}^m$ is estimated by a sum of kernel functions K [19] depending on sample realizations $\mathbf{x}_1, \ldots, \mathbf{x}_n \in \mathbb{R}^m$ (see Fig. 3(a)):

$$f(\mathbf{x}) = \frac{1}{n} \sum_{i=1}^{n} |\mathbf{H}|^{-1} K(\mathbf{H}^{-1}(\mathbf{x} - \mathbf{x}_i))$$

where $|\mathbf{H}|$ denotes the determinant of the bandwidth matrix $\mathbf{H}$ [20].

In the one-dimensional case the bandwidth matrix is reduced to a scalar bandwidth h. Several kernel functions K are conceivable [19]. In the following the considerations will be limited to the Gaussian kernel (one-dimensional case):

$K(t) := \frac{1}{\sqrt{2\pi}} e^{-0.5 \cdot t^2}$ for $t \in \mathbb{R}$ As the determination of the bandwidth $\mathbf{H}$ is usually of major importance, various methods for bandwidth determination can be found [18,21,22]. A plug-in based

method will be the one of choice as can be seen below [20]. The treatment of variables, which are subject to physical boundaries (e.g. battery cycle number ≥ 0), has to be mentioned first. As the provided definition of kernel density estimation does not take such restrictions into account (the density function f is defined in $\mathbb{R}$), explicit treatment of the boundary has to be done.

The methods 'cut and renormalize' (sparse data density in the boundary vicinity) as well as reflection are employed as described in [18].

In order to perform kernel density estimation for two-dimensional data $\mathbf{x}_i := (x_i, y_i)^T \in \mathbb{R}^2$ (see Fig. 3(b)), frequently approaches including product kernels are chosen [23]. However, by using the full bandwidth matrix $\mathbf{H} := \begin{pmatrix} h_1 & h_{12} \\ h_{12} & h_2 \end{pmatrix}$, the shape of the kernel function can be adjusted to the data structure. For diagonal bandwidth matrices ($h_{12} = 0$), h_1 and h_2 can be received via the normal reference rule: $h_1 = n^{-1/6} \cdot s_x$ and $h_2 = n^{-1/6} \cdot s_y$ where s_x and s_y denote the standard deviation of the x- and y-component [22]. Diagonal bandwidth matrices correspond to the product kernel of two one-dimensional kernels [20]. Taking into account the correlation r within the data, the shape of the kernel can be adjusted to the orientation of the data. Using a generalized version of Scott's rule for two dimensions ($\mathbf{H} = n^{-1/6} \cdot \Sigma^{1/2}$, where Σ denotes the empirical covariance matrix [24]) it can be shown for the two-dimensional Gaussian kernel that

$$K_{\mathbf{H}}(\mathbf{x}) := K(\mathbf{H}^{-1}\mathbf{x}) := K\left(\mathbf{H}^{-1} \begin{pmatrix} x \\ y \end{pmatrix}\right) = \frac{1}{2\pi \cdot h_1 h_2 \sqrt{1 - r^2}}$$

$$\cdot \exp\left(\frac{-0.5}{1 - r^2} \cdot \left(\frac{x^2}{h_1^2} - 2r\frac{xy}{h_1 h_2} + \frac{y^2}{h_2^2}\right)\right)$$

with h_1, h_2 like in the case of diagonal bandwidth matrices. This technique of data evaluation was applied for the estimation of customer distributions of driving parameters in [18] first.

3.2. Kernel density estimation of FOT data

In this publication the technique was adopted to the battery FOT data. It is exemplarily demonstrated in Fig. 4. Diagram (a) is a scatter plot depicting the relative capacity of VRLA–AGM batteries under BER conditions in pre-series vehicles (75 test runs) as a function of accumulated cycling number. By the red lines the huge scattering range is highlighted. It comes from the complexity of the system vehicle/battery and several external influences like temperature profile, driving profile and load profile of electrical consumers. At least, a linear regression fit displays a capacity loss of about $15\% \cdot C_{\text{nom}}/100$ fc. The standard deviation accounts for about 2.5%. This deviation can be regarded as acceptable for such a field test, which is also true for the limits of the fitted 95% confidence region. By the special implementation of the field test, the scattering was implicitly reduced since batteries with insufficient C_{act} in the intermediate analysis were not further tested. According to the schematic illustration in Fig. 3(b), the two-dimensional kernel density estimation was applied to the data in Fig. 4(a) resulting in Fig. 4(b). Here, the density estimate is colour-coded. At a first glance, the benefits of this kind of presentation are obvious: The density of data points is indicated by the colour in a red-blue gradient (blue: low density, red: high density). Areas with high/low density incorporate many/few data points per area unit (corresponding to high/low relative frequencies). Iso-lines indicate regions where relative frequencies are equal within very small neighborhoods, i.e. the probability density function has the same value. The integral of the density function over a certain area (volume under the graph of the density function) corresponds to a cumulative frequency, i.e. the probability within that area. The scattering area appears as a
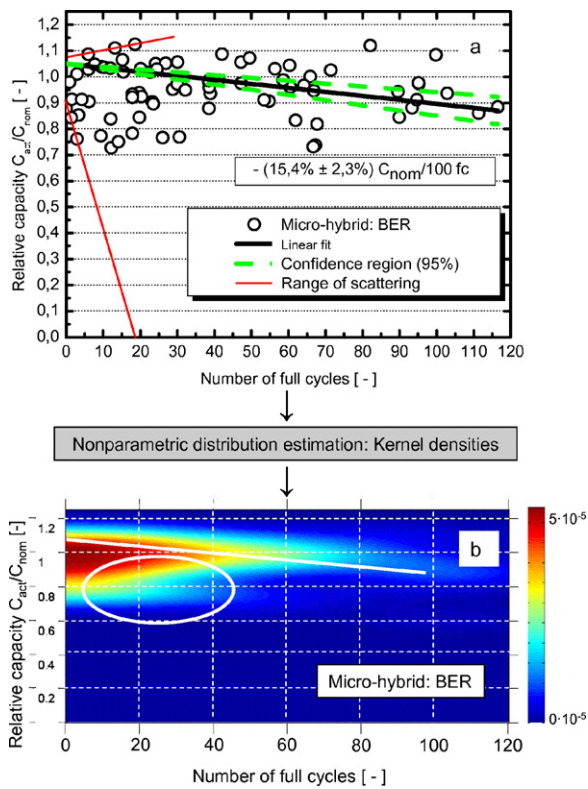
Fig. 4. (a) Scatter plot of capacity loss of BER test batteries. The range of spreading allows – if at all – a linear trend line (75 test runs). (b) Data presentation of the same data set according to the described two-dimensional kernel density estimation. The colour coding of the probability density enables clear visualisation of the scattering area and trends (indicated white).

Fig. 5. (a) Capacity loss of VRLA–AGM batteries in the CPS (51 test runs) compared to the MHPS (36 test runs). There is no significant difference of capacity loss detectable. The contour lines are widely broadened due to immense scattering. Nevertheless, a bi-trend is visible, which is linked to the mileage performance of the underlying fleets. Normalised to the driving profile, the capacity loss should be pronounced in the MHPS as is discussed later. (Outermost contour line and spacing between contour lines of probability density: 0.5×10^{-5}.) (b) Batteries operated at pSoC (106 test runs) are compared to a benchmark group of striking durable returned batteries from the CPS field (59 batteries). (Outermost contour line and spacing between contour lines: 2.0×10^{-6}.)

homogeneous area, which has a smooth shape instead of discrete data points. This kind of presentation still incorporates the trend of about 15% capacity loss per 100 fc (white line), which was also described by the scatter plot. Furthermore, multiple trends, which might occur in the field, are better recognized (white circle) in contrary to a standard scatter plot. The only missing information – the absolute number of contributing data points – has to be given separately.
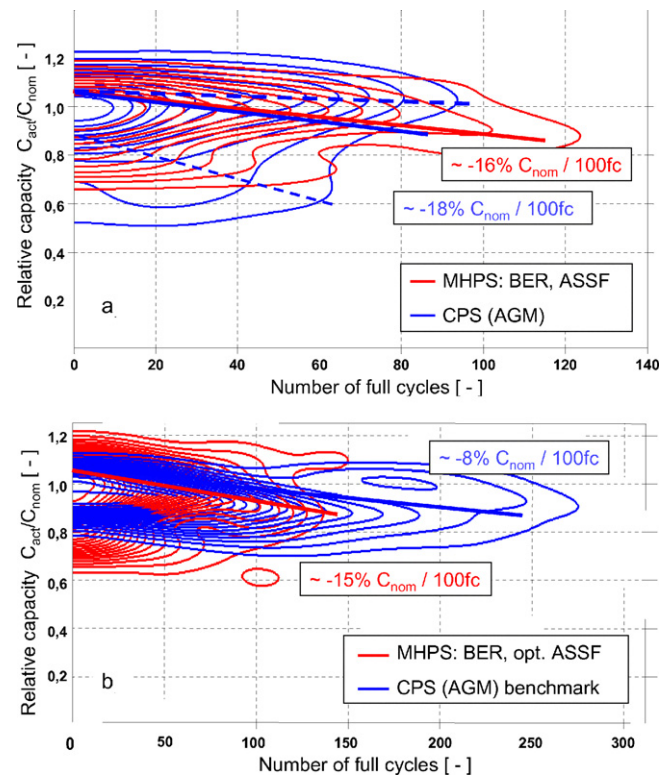
Non-interferential statements about trends, deviations from those and variation (given by the experimental conditions) are allowed for the chosen visualization. The described method is also suitable for the co-visualization of different datasets. Conditional distributions, relative frequencies and resulting variations are visualized in the regarded parameter regions.

4. Results and interpretation

VRLA–AGM batteries and flooded batteries operated in the MHPS and CPS are discussed according to the introduced analysis method. This covers charge acceptance, cold cranking performance and capacity loss. In order to compare two data sets of density estimates, contour lines representing regions of equal relative frequency were introduced in different colours.

4.1. Capacity loss

In Fig. 5(a) the relative capacity C_{act} with respect to C_{nom} is depicted by density iso-lines versus the number of cycles. The red contour lines depict a dataset of 36 test runs in the MHPS (BER and ASSF) of pre-series vehicles. They are compared with VRLA–AGM batteries operated in the CPS (blue, 51 test runs), mainly operated

in series vehicles of the VIP fleet or in new police cars with available info memory entries. In both cases the scattering is enormous. The fitted capacity losses with about $-17\% \cdot C_{nom}/100$ fc (linear fits as in Fig. 4(a)) are not distinguishable from each other at the given accuracy of about $\pm3\%$. It might be deduced from this fact that there is no additional battery stress for VRLA–AGM batteries in the MHPS compared to the CPS. This aspect will be picked up in a later discussion of the underlying driving profiles. In this context also the bi-trend (dashed lines) that develops at low relative capacities in the CPS will be discussed.

In Fig. 5(b) the capacity loss of 106 test runs in the MHPS is depicted (pre-series vehicles). The capacity loss accounts for $-15\% \cdot C_{nom}/100$ fc (red). The main difference to the MHPS test runs depicted in Fig. 5(a) is the take rate of ASSF, which is only about 30% in Fig. 5(b). Despite of this, the capacity loss is comparable to the MHPS vehicles in Fig. 5(a) with 100% ASSF. This leads to the conclusion that ASSF does not significantly stress the batteries in dependence of cycling number provided that the battery is operated at pSoC in any case. However, it has to be noted that the cycling rate with reference to mileage is higher in presence of ASSF, of course.

In Fig. 5(b) a benchmark of VRLA–AGM batteries operated in CPS cars is indicated by blue contour lines (59 batteries). These batteries serve as a reference group and were operated in customer vehicles. They were electrically measured after their return from the field according to a battery return process (no breakdowns). The number of full cycles was derived from the vehicle info recorder protocol like from the FOT batteries. Analogous to the procedure described
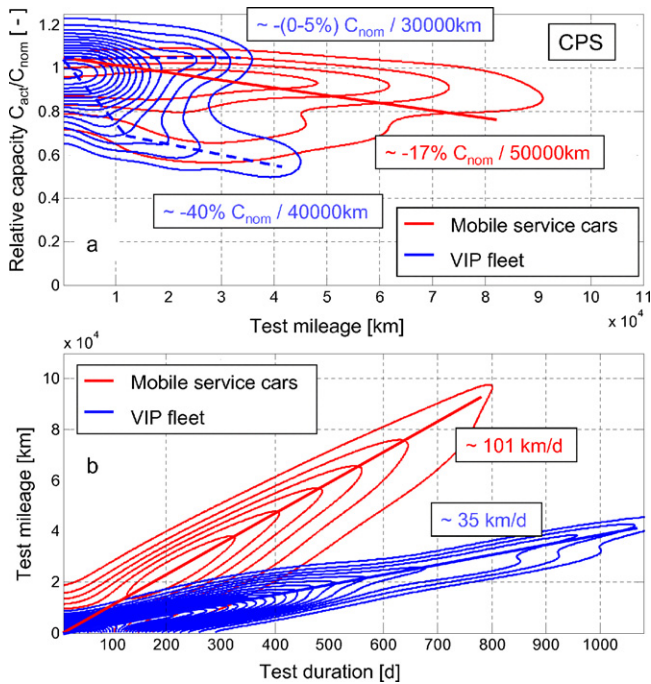
Fig. 6. (a) Capacity loss of VRLA–AGM batteries in CPS vehicles of different fleets. (Outermost contour line and spacing between contour lines of probability density: 1.0×10^{-5} km^{-1}.) (b) The varying mileage performance (factor 3 between VIP vehicles in blue, 69 test runs, and mobile service cars in red, 47 test runs) has great impact on the progress of capacity loss. (Outermost contour line and spacing between contour lines: 1.0×10^{-5} km^{-1} d^{-1}.) A clear bi-trend and large scattering is observed for VIP fleet vehicles in (a). The lower branch reflects a strong capacity loss ($-40\% \cdot C_{nom}/40,000$ km). This is most likely caused by extended vehicle rest time (see also [10]). (For interpretation of the references to colour in this figure legend, the reader is referred to the web version of the article.)

in Section 3.1, only the batteries with at least 70%·C_{nom} remaining capacity were used for the kernel estimation in Fig. 5(b) in order to ensure comparability. It is clearly proven that VRLA–AGM batteries allow more than 240 fc at still 80% of their capacity (average capacity loss of about $-8\% \cdot C_{nom}/100$ fc). A full interpretation can only be given against the background of the driving profile. The batteries were operated at moderate temperature with lots of extra-urban vehicle operation and without extensive rest times in between (average mileage about 150 km d^{-1}).

The enormous influence of the mileage performance is illustrated by Fig. 6. VRLA–AGM batteries were operated in CPS vehicles of two different fleets (mobile service cars and shuttle service cars). As depicted in Fig. 6(b) both vehicle groups represent a quite homogeneous, but differing mileage performance. The blue contour lines represent test runs in the VIP fleet (69 test runs). The average mileage of the VIP fleet amounts to 35 km d^{-1}. The scattering with ± 1.1 km d^{-1} is quite low and the annual mileage of about 12,800 km meets the average customer mileage in good agreement [25]. In contrast, the annual mileage of the service mobiles (red contour lines) compared to the VIP fleet is increased by a factor of three (36,900 km) with an average daily mileage of 101 ± 4.2 km (47 test runs). After 50,000 km about $17 \pm 2.4\%$ of the nominal capacity is lost (Fig. 6(a)). Note that the y-intercept is fixed at $1.05 \cdot C_{nom}$, which is a value of experience for brand-new batteries. The contour lines of the mobile service fleet clearly show the experimental boundary conditions of the field test: There is a minimum of relative capacity at about 30,000 km test mileage (lowest red contour line).

A more serious capacity loss at higher mileage is not observed since 'bad' batteries were sorted out after the intermediate analysis as mentioned above. The service-shuttle vehicles reveal another remarkable effect although the total mileage reached only up to

45,000 km due to lower annual mileage. About half of the battery test runs do not show any capacity loss—at least up to a mileage of 30,000 km. So far, this does not differ from the evolution of the service mobile data. However, after about 10,000 km a clear bi-trend is observed. The contour lines form a separate branch which indicates a distinct capacity loss of $-40\% \cdot C_{nom}/40,000$ km. Again, the experimental conditions act as lower limit.

The observed phenomenon is exclusively related to the mileage performance in the VIP cars for the following reasons: The cycling rate (fc per mileage) is even higher in the service mobile cars because of the additional diagnosis equipment. Several model types contributed to the shuttle-service data, thus specific reasons for a particular model type (e.g. increased quiescent current) are not essential. And the batteries types of different manufacturers were mixed in both fleets. Thus, it can be interpreted that the mileage performance of 35 km d^{-1} lies obviously in a range, which marks unfavourable operating conditions. Two problems arise in case of low mileage performance. If the profile is characterized by many short trips, the charge balance is negative for each trip. Pre- and post-drive phases, which go along with any short trip result in battery charge depletion and, thus, capacity loss. Furthermore, extensive intermediate rest periods seriously damage the battery due to self-discharge and – as a consequence – deep discharge and sulphation. If, in contrast, long trip runs are made, the battery is occasionally fully charged with respect to its charge factor.

With the insights of Fig. 6 the comparative interpretation of the capacity loss in the MHPS and CPS (Fig. 5) can be resumed. For both groups the capacity degrades with formation of a second branch to lower capacities (e.g. lower dashed blue line in Fig. 5(a). It was mentioned that the pre-series vehicles were operated extensively. The scattering range is enormous, it reaches from 10 to 600 km d^{-1} and the average is 200 km d^{-1}. Therefore, a simple cluster analysis was performed: All test runs with an average mileage of more than 400 km d^{-1} end up in the upper branch—even if the C_{20} capacity of the battery was worse in the intermediate analysis than before it was mounted. The inversion of the argument did not match perfectly. It was found that all test runs with an average mileage below 50 km d^{-1} terminated with lower C_{20} capacity compared to the intermediate analysis before the test run, but did not automatically end in the lower branch of capacity loss. However, this could be related to the constraints of the FOT. Most test runs did not take more than six months and a battery may have been brand-new or rotated from a vehicle with low mileage performance to a vehicle with higher mileage performance and vice versa.

The main conclusion refers to the average capacity loss of both groups as indicated by the linear fits in Fig. 5(a). The average mileage of the VRLA–AGM batteries operated in the MHPS is significantly higher than for the VRLA–AGM operated in the CPS (200 km d^{-1} versus 50 km d^{-1}). Therefore, it has to be assumed that the capacity loss of VRLA–AGM operated in the MHPS is enhanced if the driving profile is normalized to the VRLA–AGM batteries operated in the CPS. However, this effect is hard to quantify because of interference with the battery refresh function, which is triggered (besides others) at low SoC in the MHPS. It was demonstrated in [3] that the refresh function has detectable positive influence on the short term and long term operational behaviour of the battery.

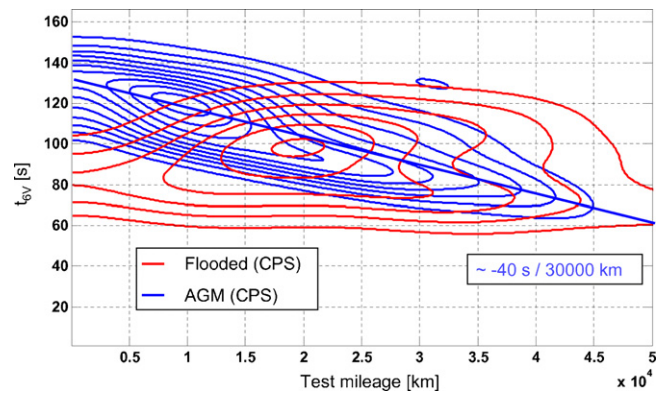### 4.2. Comparison of VRLA–AGM and flooded batteries

The challenges for LA batteries in the MHPS were described in section 1. Therefore, only VRLA–AGM batteries were applied in BMW micro-HEVs. The presented FOT enabled a comparison of VRLA–AGM batteries and flooded batteries in the CPS from which the superiority of VRLA–AGM batteries can be derived. Capacity loss and cold cranking performance are briefly discussed.
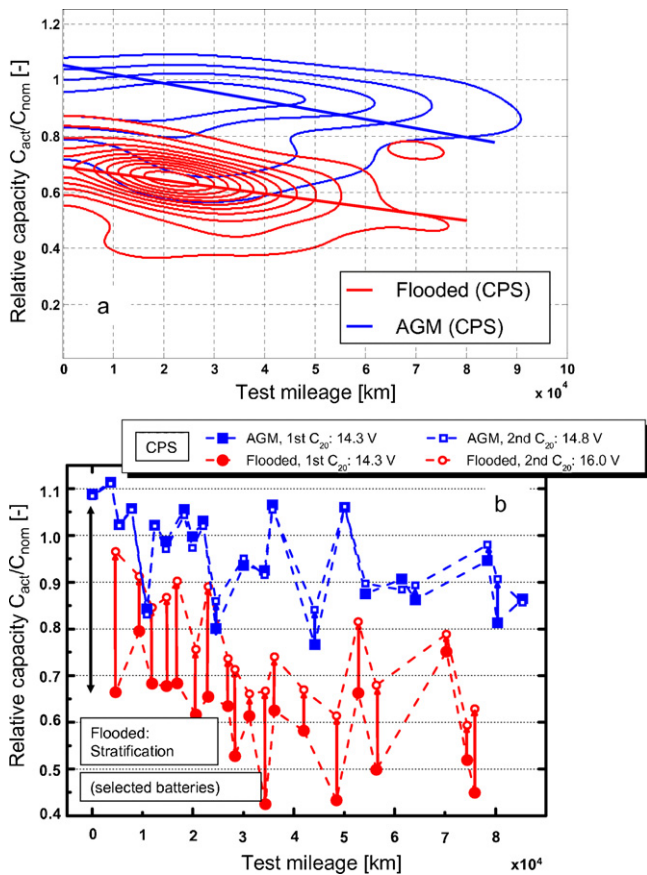
Fig. 7. (a) Capacity loss of VRLA–AGM (47 test runs) and flooded batteries (57 test runs) in the same field test fleets. (Outermost contour line and spacing between contour lines of probability density: 1.0×10^{-5} km^{-1}.) A clear initial capacity loss of flooded batteries is found due to acid stratification. The lower limit is given by the experimental conditions. (b) The early capacity loss of flooded batteries is partially reversible by charging with 16 V.


Fig. 8. The parameter t_{6V} of 90 Ah VRLA–AGM batteries (40 test runs) is limited by the amount of electrolyte. As flooded batteries (here 110 Ah, 30 test runs) are produced with a surplus of electrolyte, the current load capability in maintained versus mileage. (Outermost contour line and spacing between contour lines of probability density: 1.0×10^{-5} km^{-1} s^{-1}.)

In Fig. 7(a) the relative capacity is given versus test mileage in the CPS. Flooded batteries of different sizes and manufacturers (70, 80, 90 and 110 Ah) are shown in red (57 test runs), VRLA–AGM batteries (70, 80 and 90 Ah) in blue (47 test runs). Note that the influence of the driving profile does not result in any additional differences between VRLA–AGM and flooded batteries because both technologies were randomly mounted in the police fleet, the VIP shuttle-service cars and service mobile cars. The VRLA–AGM batteries show only a moderate capacity loss ($-17.6 \pm 2.5\% \cdot C_{nom}/50{,}000$ km) as was found also in Fig. 6(a).

It is remarkable that the intersect of the curve with the y-axis at $105\% \cdot C_{nom}$ is inappropriate for the flooded batteries. Obviously they suffer from a very early capacity loss already after a few full cycles. This capacity loss is supposed to be caused by acid stratification and reaches an equilibrium obviously within the first cycles of operation. Linear fitting with variable y-intercept displays a weak capacity loss of only $-9.4 \pm 3.7\% \cdot C_{nom}/50{,}000$ km. However, the resulting early capacity loss, which is represented by the fitted y-intercept and the initial capacities, results in $-38.1 \pm 2.6\%$ in relation to the initial values. If this early capacity loss is taken into account for fitting, the capacity loss of flooded batteries after 50,000 km is found as about -47.5%. It can be nicely seen from the bottom contour lines of the flooded batteries that the scattering area has a lower limit again. This is set by the experimental conditions as was mentioned before, the upper limit comes from acid stratification as will be proven in Fig. 7(b). Here, both the capacity measurement after charging with 14.3 V and after repeated charg-

ing with 16 V are depicted. The according data visualization was made for VRLA–AGM batteries after charging with 14.3 and 14.8 V, respectively. Only few batteries were selected randomly in order to keep the illustration clear. It is observed that a capacity band spans in case of the flooded batteries since the second full charging with 16.0 V has a tremendously positive effect on the capacity. Particularly, the capacity improves by about 20%, at least by about 5%—which is roughly the maximum improvement for VRLA–AGM batteries after IU-charging with 14.8 V. In flooded batteries the stratification of the electrolyte, but also resulting plate stratification due to plate-internal charging, i.e. particularly sulphation of the NE in the lower part, are partially reversed by overcharging at elevated voltage. The acid intermixes due to rising gas bubbles (gassing reaction) and the higher overvoltage induces recharging of PbSO$_4$ crystals with poor surface to mass ratio. This refresh effect is not realizable in the vehicle application. Neither a charge voltage of 16 V nor an uninterrupted charging for 24 h is randomly feasible.

In Fig. 8 the time until 6 V is reached at discharge with 60% CCA (t_{6V}, an important parameter reflecting cold cranking performance according to [15]), is comparatively depicted at $T = -18$ °C. The underlying datasets do not exactly correspond to Fig. 7(a), as only the 110 Ah flooded and 90 Ah VRLA–AGM batteries are shown. After a mileage of 50,000 km, the current load capability of flooded batteries does not significantly change versus cycling/mileage. The scattering range reaches from 60 to 130 s. The initial ability of the VRLA–AGM battery to supply high current lasts about 60 s longer due to its power-optimized design. With increasing mileage the t_{6V} of VRLA–AGM batteries reveals a decrease of -59.0 ± 10.3 s/50,000 km. As a result, after 50,000 km the VRLA–AGM batteries break even with the flooded ones. It has to be kept in mind that the test current for the VRLA–AGM battery is 30 A higher and it is more than 1 kg lighter. The reason for the decreasing high-rate performance of the AGM type is its electrolytic limitation, i.e. its lower ratio of electrolyte/active masses. VRLA–AGM batteries are very sensitive to the saturation degree of the separator with electrolyte. If, in the course of battery operation, a certain amount of electrolyte is lost by, e.g. water consumption or plate sulphation, an immediate impact on the t_{6V} parameter occurs [10]. During discharge acid depletion in the pores of the active mass (AM) arises and the voltage drops to a lower level more rapidly although available AM has not yet fully reacted.

Nevertheless, with respect to cranking capability, represented as U_{10s}, the 110 Ah flooded batteries reveal disadvantages compared to the AGM type. Fig. 9(a) depicts test runs of both battery technologies with comparable cycling rate. Test runs in the range of 0.75–1 fc/1000 km were selected (31 test runs with flooded and
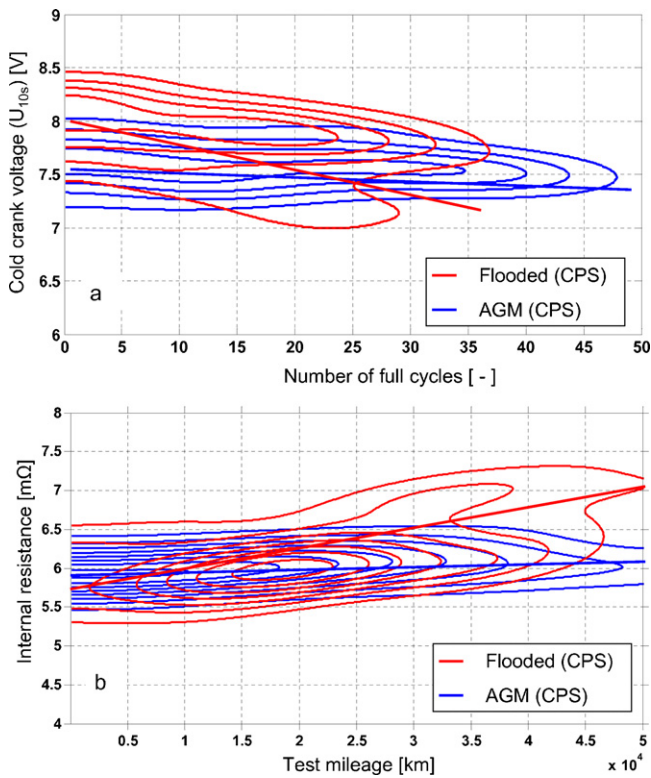
Fig. 9. (a) Cold cranking voltage, U_{10s}, and the corresponding internal resistance, R_i, (b) are nearly constant for VRLA–AGM batteries (40 test runs). Flooded batteries (28 test runs) exhibit inferior performance after about 15–25 fc. In terms of MHPS application, the U_{10s} is more relevant than the t_{6V}. (a) Outermost contour line and spacing between contour lines of probability density: 1.0×10^{-5} V^{-1}. (b) Outermost contour line and spacing between contour lines: 0.5×10^{-5} V^{-1} mΩ^{-1}.

VRLA–AGM batteries), also the mileage performance was comparable. Both the U_{10s} (a) and the internal resistance (b) stay nearly constant in the case of AGM batteries. On the time scale of a few seconds, especially on the time scale of high-current load during warm cranking, the described acid limitation of the VRLA–AGM type is not a determining factor. Instead, its power optimization becomes evident. After about 20,000 km some samples of the flooded batteries already exhibit an increased internal resistance and decreased cold cranking voltage. The resulting slope is -0.27 ± 0.02 V/25 fc. Usually, the most prominent reason for this behaviour in flooded batteries is vanishing adhesion of positive AM to the grid.

4.3. Charge acceptance of VRLA–AGM batteries

It was presented in the introductory section of this publication that the dynamic charge acceptance (DCA) is a key parameter of LA batteries in the MHPS. It was demonstrated in [3] that the refresh function is able to improve charge acceptance (CA). Although AGM batteries with higher CA compared to flooded ones are applied, the efficiency of BER is limited by degrading CA during cycle life of the batteries. In the course of this section two types of charge acceptance measurements are discussed as part of the FOT.

The first charge acceptance test (CA test I) was performed directly after an OCV measurement at the beginning of every laboratory analysis. The rest time t_{rest} after dismounting until arrival checking in the laboratory varied from about 6 h to maximum three weeks due to battery transport and storage. In the CA test I the battery is IU-charged for 60 s at 14.8 V and 200 A maximum current at room temperature. The charge current is detected as
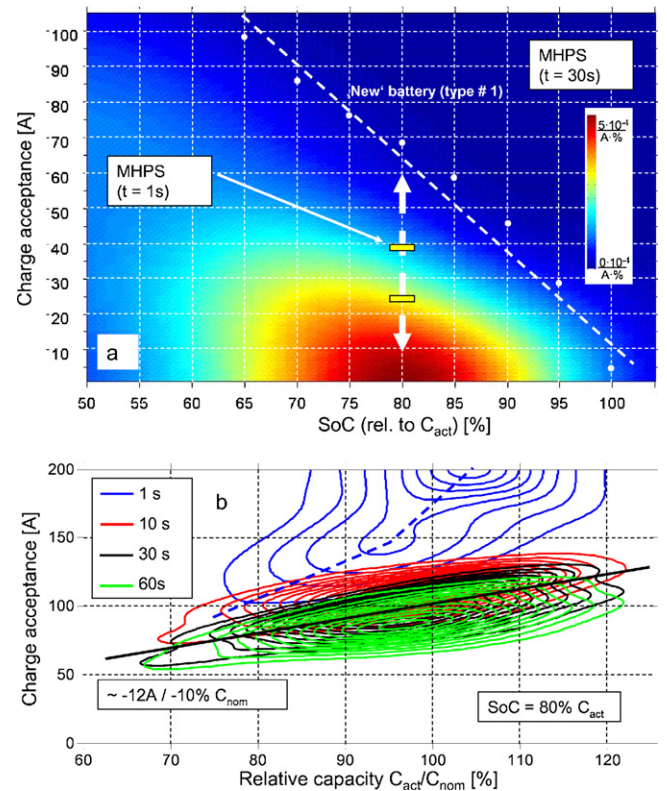
Fig. 10. (a) Battery DCA after dismounting (and varying t_{rest}) is presented after charge time of 30 s with 14.8 V. Roughly half of the batteries (37 test runs) reveal DCA worse than 20–25 A. After 1 s charge time the corresponding value is close to 40 A, whereas a brand-new battery accomplishes nearly 70 A. (b) The correlation between capacity loss and decrease of DCA is investigated by the 'charge acceptance II' test. It is about 12 A per 10% lost capacity at SoC = 80% and the given experimental conditions. (Outermost contour line and spacing between contour: 1.0×10^{-4} A%$^{-1}$.)

a function of charging time. The actual SoC of the CA test I is determined retrospectively in the course of the further test procedure.

In Fig. 10(a) the 'charge acceptance I' of VRLA–AGM batteries (90 Ah, 37 test runs in pre-series vehicles, see also Fig. 5(a)) operated in the MHPS is given versus SoC. The value of charge current refers to 30 s charge time. By the way of measurement this reflects the CA as it would have occurred in the vehicle (after the same vehicle rest time). The focal point of the distribution (highest probability density) is at 5–10 A charge acceptance (and at SoC $\approx$ 80% due to the pSoC operational strategy). The yellow zone roughly divides the number of samples in halves (after 2D-integration of the density). At SoC = 80% it lies at 20–25 A after 30 s charging (yellow flag). Of course, the average charge acceptance during a 30 s coasting phase is significantly higher because the initial charge acceptance (at 1 s charge time) is approximately twice as high. This is also indicated in Fig. 10(a) by the second yellow flag which marks the corresponding charge acceptance after 1 s charge time for the same batteries. As a reference the corresponding CA I was also measured for a brand-new battery (6 h rest time after SoC conditioning by discharging). As shown in [10] the compliance of the rest time is very critical since DCA $\sim -\ln(t_{rest})$. The variation of t_{rest} can be interpreted as systematic error of the presented FOT, but could not be prevented for practical reasons. However, the main outcomes are not affected: DCA during operation at about 80% pSoC strongly suffers for batteries with still at least 70%·C_{nom}. At worst, it reaches less than one third for half of the batteries compared to a brand-new battery in conventional operation. This has to be interpreted as lower limit since the reference battery accomplished not more than 6 h t_{rest} before the

CA test I. Moreover, the CA I test was performed following a discharge step. This additionally favors CA according to Sauer et al. [13]. Anyway, DCA outlines a major potential for optimizations of the LA technology for micro-hybrid application in the next future. It vanishes disproportionately fast in comparison to capacity. This is demonstrated by the second charge acceptance test (CA test II).

The CA test II is performed after determination of the actual capacity, C_{act}, by a C_{20} measurement. After charging with 14.8 V the SoC is conditioned to 80% (by discharging) and the battery is – immediately afterwards – IU-charged for 60 s at 14.8 V and maximum current of 200 A at room temperature (like CA test I). The charge current is shown in Fig. 10(b) after different charge time of the 14.8 V charge step. The abscissa depicts the relative capacity. At first, the focal point of the 1 s-data is located at 105%·C_{nom}, which was set as fixed y-intercept in linear fits of capacity loss in the previous figures. DCA at 1 s charging time covers a range from 100 to 200 A, which is the upper limit due to the experimental instrumentation. As a result, a bitrend is observed (kinked dashed line). The weaker slope indicates about 20 A lost CA per 10% lost capacity. For the 10, 30 and 60 s values the loss of DCA is quite similar and accompanied by weak scattering. For the three parameters it accounts for −12 A/−10%·C_{nom} in average. In case of the 30 s-data, 12 A reflect about 10% of the maximum DCA (at 105% relative capacity), i.e. 10% DCA vanishes with about 10% lost capacity. However, this has to be interpreted as best case conditions as the CA test II is done after a C_{20} capacity measurement and with subsequent fully charging. As discussed in [3,10] this has drastic influence on the battery and improves especially the DCA—similar to the refresh function. Furthermore, no t_{rest} between SoC adjustment and DCA measurement was included—thus the highest possible DCA was measured. Consequently, these results are only hardly transferable into the situation of the vehicle. The focal point of the 30 s-data is located at 95% relative capacity and 90 A DCA in part (b) of Fig. 10, whereby the corresponding value in (a) is 10 A instead. In spite of this, it is clearly shown by Fig. 10 that both the absolute DCA level at modern automotive operational scenarios and its robustness against battery degradation have to be considered as main challenges for the present LA battery technology. In terms of ASSF low internal resistance is a fundamental requirement in addition.

5. Summary

A battery field operational test on VRLA–AGM and flooded batteries in conventional and micro-hybrid electric vehicles was presented. The results were presented by the use of a continuous method, a nonparametric two-dimensional kernel density estimation instead of scatter plots or histograms. Thus, different statistically relevant data sets could be compared. It was found that capacity loss of AGM batteries is enhanced in the MHPS. Exact quantification is not possible because of the interference of mileage performance and the refresh function. It was demonstrated that VRLA–AGM batteries are advantageous compared to flooded batteries. These suffer from a very early capacity loss due to acid stratification already in the less challenging CPS and show stronger increase of internal resistance. For ASSF a possibly low internal resistance is desired. In general, a great optimization potential of LA batteries is given by restricted dynamic charge acceptance. In vehicle operation it decreases considerably faster than battery capacity on relative scale. This may hinder innovative attempts to further integrate the LA battery as active component in the automotive power net. However, the trade-off between durability, reliability, power and energy density, costs and safety makes the VRLA–AGM batteries to the state-of-the-art energy storage device in modern passenger vehicles. In part II of this publication selected FOT data are presented by the use of multiple regression analysis.

References

[1] S. Schaeck, T. Karspeck, C. Ott, D. Weirather-Koestner, A.O. Stoermer, Journal of Power Sources 196 (2011) 2933–2938.
[2] C. Diegelmann, J. Stauber, M. Hafkemeyer, S. Wolff, Proceedings of the 7th International Advanced Automotive Battery Conference, Long Beach, May 2007.
[3] S. Schaeck, A.O. Stoermer, E. Hockgeiger, Journal of Power Sources 190 (2009) 173–183.
[4] H.A. Catherino, F.F. Feres, F. Trinidad, Journal of Power Sources 129 (2004) 113–120.
[5] S. Wolff, D. Abendroth, W. Weigl, C.-P. Linner, R. Neudecker, M. Schneider, W. Huber, A. Rau, Proceedings of the 7th Stuttgart International Symposium Automotive and Engine Technology, Stuttgart, Germany, March 2007.
[6] M. Hafkemeyer, F. El-Dwaik, A. Heim, J. Liebl, J. Stauber, F. Traub, Proceedings of the 12th International Conference on Electronic Systems for Vehicles, Baden-Baden, October 6–7, 2005.
[7] M. Schmid, M. Schöllmann (Eds.), Energiemanagement und Bordnetze II, Haus der Technik Fachbuch, Expert Verlag, Germany, 2007.
[8] E. Karden, S. Ploumen, E. Spijker, D. Kok, D. Kees, P. Phlips, M. Schöllmann (Eds.), Energiemanagement und Bordnetze, Haus der Technik Fachbuch, Expert Verlag, Germany, 2004.
[9] F. Dudenhöffer, M. Krüger, H. Schmaler, ATZ 106 (2004) 42–45.
[10] S. Schaeck, A.O. Stoermer, F. Kaiser, L. Koehler, J. Albers, H. Kabza, Journal Power Sources 196 (2011) 1541–1554.
[11] E. Karden, P. Shinn, P. Bostock, J. Cunningham, E. Schoultz, D. Kok, Journal of Power Sources 144 (2005) 505–512.
[12] R.F. Nelson, Journal of Power Sources 107 (2002) 226–239.
[13] D.U. Sauer, E. Karden, B. Fricke, H. Blanke, M. Thele, O. Bohlen, J. Schiffer, J.B. Gerschler, R. Kaiser, Journal of Power Sources 168 (2007) 22–30.
[14] P.T. Moseley, Journal of Power Sources 127 (2004) 27–32.
[15] German standard DIN EN 50342-1 (2006).
[16] M. Mauerer, Monitoring of 12V Lead-Acid-Batteries in Micro Hybrids, Proceedings of the AABC Europe 2010, Mainz, Germany, 2010.
[17] R. Naumann, M. Schöllmann (Eds.), Energiemanagement und Bordnetze, Haus der Technik Fachbuch, Expert Verlag, 2004.
[18] T. Karspeck, T. Klaiß, H. Zellbeck, Proceedings of the '9. Internationales Stuttgarter Symposium', Stuttgart, 2009.
[19] B. Silverman, Density Estimation for Statistics and Data Analysis, Chapman and Hall, London, 1986.
[20] M. Wand, M. Jones, Kernel Smoothing, Chapman and Hall, London, 1995.
[21] D. Korus, Selektivitätsabschätzung von Bereichsfragen auf metrischen Attributen mit nichtparametrischen Verfahren, PhD thesis, Universität Marburg, 2000.
[22] D. Scott, Multivariate Density Estimation: Theory, Practice and Visualization, Wiley & Sons, New York, 1992.
[23] L. Fahrmeir, R. Künstler, I. Pigeot, G. Tutz, Statistik–Der Weg zur Datenanalyse, Springer-Verlag, Berlin, 2007.
[24] W. Härdle, M. Müller, S. Sperlich, A. Werwatz, Nonparametric and Semiparametric Models, Springer-Verlag, Berlin, 2004.
[25] Deutsches Institut für Wirtschaftsforschung, Fahrleistungen und Kraftstoffverbrauch im Straßenverkehr, Wochenbericht des DIW Berlin (51), 2002.